Dynamical origins of weakly coupled relaxor behavior in Sn-doped (Ba, Ca)TiO_3-$BiScO_3$

A. Pramanick,[1,*] S. Nayak,[1] T. Egami,[2] W. Dmowski,[2] A. Setiadi Budisuharto,[1] F. Marlton,[3,†] M. R. V. Jørgensen,[3,4] S. Venkateshwarlu,[1] and K. A. Beyer[5]

[1]*Department of Materials Science and Engineering, City University of Hong Kong, Hong Kong SAR, China*
[2]*Shull Wollan Center, Oak Ridge National Laboratory, Oak Ridge, Tennessee 37831, USA and Department of Materials Science and Engineering, University of Tennessee, Knoxville, Tennessee 37996, USA*
[3]*Center for Materials Crystallography, Department of Chemistry and iNANO, Aarhus University, 8000 Aarhus C, Denmark*
[4]*MAX IV Laboratory, Lund University, SE-221 00 Lund, Sweden*
[5]*Advanced Photon Source, Argonne National Laboratory, Lemont, Illinois, USA*

(Received 26 July 2020; revised 3 December 2020; accepted 19 May 2021; published 4 June 2021)

The peculiar characteristics of relaxors, viz., a frequency-dependent dielectric permittivity peak and good functional properties (dielectric, electromechanical, electrocaloric, etc.), are attributed to nanoscale regions with correlated dipoles, or polar nanoregions (PNRs). However, the exact nature of PNRs and their contribution to relaxor behavior remains debatable. In recent years, solid solutions of $BaTiO_3$-$BiMeO_3$ (where Me is a metal), have emerged as an interesting system with characteristics in between that of relaxors and dipole glasses. Here, we have examined the atomistic origins of weakly coupled relaxor behavior, specifically with regard to formation of PNRs, in Sn-doped $(1-x)$(Ba, Ca)TiO_3-$x$$BiScO_3$ using macroscopic polarization and neutron dynamic pair distribution function measurements. We show that the short-range atomic correlations observed within the PNRs dynamically fluctuate with frequencies of the order of THz. Furthermore the composition-dependent dielectric and polarization behaviors are critically influenced by the relative stability of the atomic correlations near ~1 THz, while the instantaneous atomic correlations are largely independent of x. The current results are discussed based on a model of intrinsic local modes distributed in a dielectrically soft matrix.

DOI: 10.1103/PhysRevB.103.214105

I. INTRODUCTION

Ferroelectrics are materials with a spontaneous polarization, which can be switched under the application of an electric field [1]. Relaxors are a subclass of ferroelectric materials, which are characterized by a broad dielectric permittivity spectrum as a function of temperature, a strong frequency dependence of the temperature for maximum permittivity (T_m), and deviation from the Curie-Weiss law [2–6]. They are of interest in several electronic applications due to their uniquely high dielectric constant as well as large electromechanical and electrothermal properties [7–10]. The peculiar physical characteristics and excellent functional properties of relaxor ferroelectrics are generally attributed to the presence of nanoscale domains with locally correlated polarization, otherwise known as polar nanoregions (PNRs) [4,11,12]. Despite considerable research over the last decades, the physical mechanisms governing the *formation* of PNRs are not fully understood.

Initial studies on Pb-based relaxors, such as Pb(Mg, Nb)O_3 (PMN), emphasized the role of random fields towards the formation of nanoscale domains or polar clusters in compositionally heterogeneous systems. Based on statistical ideas originally put forward by Imry and Ma, [13], Kleemann proposed that PNRs are created due to extreme slowing down of dynamics in the presence of random fields [14]. Later, Pirc and Blinc proposed PNRs as reorientable polar clusters, which interact through random bonds and are embedded in an array of chemically ordered regions [15]. Then, Fu *et al.* described that the relaxor behavior in PMN is due to the presence of nanoscale inhomogeneous ferroelectric domain structure, which exists together with random fields [16]. The role of random fields is, however, more intriguing for the case of isovalent substitutions, which are more prevalent in Pb-free relaxors, viz., (K, Li)TaO_3 or Ba(Zr, Ti)O_3 [17,18]. If both the original and the substituting elements have the same valence, the occupation of these elements on the same lattice site should nominally generate few random fields. However, it is argued that weak local random fields are generated due to local modification of polarizability of the lattice in the case of isovalent substitutions [17,19,20]. Even then, it was shown for Ba(Zr, Ti)O_3 that turning off random fields does not substantially alter the dielectric susceptibility curve [21], which questions the role of random fields as a sole origin of relaxor behavior [22,23]. Instead, it was proposed that the origin of relaxor behavior can be mainly ascribed to the local interaction among nanoscale polar clusters that are formed due to the difference in ferroelectric strengths of the host Ti and substituting Zr ions [21]. Therefore, more than the random fields itself, the dynamic instability of the local polar correlations becomes important for understanding and tuning of relaxor behavior.

It was realized early that PNRs are dynamic and inclusion of dynamical effects would be necessary to clearly

*apramani@cityu.edu.hk
†Present address: School of Chemistry, University of Sydney, Australia.

 ©2021 American Physical Society

understand the mechanism for formation of PNRs [15]. Neutron backscattering and spin-echo measurements revealed slow dynamics for PNRs at GHz frequencies in Pb-based relaxors [24–26]. However, relaxational dynamics at GHz or lower frequencies is most likely associated with fluctuations of a collection of atoms, such as within PNRs, rather than local lattice dynamics. Broadband dielectric spectroscopy indicated that dielectric relaxation in relaxors could be observed even at THz frequency, which the authors attributed to dipolar fluctuations caused by phonon absorption by existing PNRs; however, the underlying physics was not clear [27,28]. In other words, these measurements inform about the dynamics of existing PNRs, rather than the underlying physical principles governing the formation of PNRs, which is the focus of the present work.

Later models emphasized the role of localized lattice vibrational modes towards PNR formation. In the model proposed by Bussmann-Holder *et al.*, the localized excitations are described as intrinsic local modes or ILMs, which are multivibrational quanta bound states of elementary local excitations [29,30]. The ILMs result from a distribution of highly polarizable dopants within a dielectrically soft matrix. Another more recent study proposed that PNRs form due to Anderson localization, which involves trapped standing waves caused by coherent multiple scattering interference from randomly dispersed dopant sites [31]. The atomistic mechanisms leading to localization of lattice dynamics was furthermore elucidated from dynamic pair distribution function (DyPDF) studies. For example, Dmowski *et al.* showed that PNRs form in PMN due to the interaction between soft phonons and local dynamic off-centering of Pb atoms [32]. Similarly, PNRs can be stabilized for an optimum addition of Zr in $Ba(Zr, Ti)O_3$, which locally alters the energy state of soft phonons and modifies their interaction with dynamic off-centering of Ti ion [33]. However, barring a few examples as listed here, the number of studies on THz atomistic dynamics that govern the formation of PNRs is rather limited. The emergence of new Pb-free relaxors in recent years provides an opportunity to further examine the dynamic models for PNR formation.

One interesting system to study the governing principles for formation of stable PNRs is the solid solutions of $BaTiO_3$-$x$$BiMeO_3$ (Me represents one or more metal ions), which are described as weakly coupled relaxors [34,35]. These systems typically exhibit a highly diffuse phase transition leading to a broad peak in the dielectric permittivity spectrum as a function of temperature, a large frequency dispersion in T_m, and higher values of activation energy for dipole reorientation as compared to some other well-known relaxors. The broadness of their temperature-dependent dielectric permittivity spectrum makes $(1-x)BaTiO_3$-$x$$BiMeO_3$ solid solutions particularly attractive for high-density energy storage applications [35–37]. Phenomenologically, the peculiar characteristics of $(1-x)BaTiO_3$-$x$$BiMeO_3$ relaxors are described as a result of weak interactions among the polar clusters, which are isolated in a dielectric matrix with dispersed random fields [34,35]. It was argued that the origin of random fields is due to the substitutions of Bi and Me at the *A* and *B* sites, respectively. Interestingly, the polarization behavior of $BaTiO_3$-$BiMeO_3$ solid solutions is strongly dependent on the concentration of $BiMeO_3$. For example, for low $x <$ 0.05, a ferroelectric behavior was reported, while for higher x polarization behavior similar to dipolar glass is observed at low temperatures [38]. It was proposed that whether a dipolar glass or polar ferroelectric state is obtained at low temperature depends on the competition between local ferroelectric order and surrounding random fields [38,39]. Alternately, an atomistic model for weakly coupled relaxor behavior was proposed by Krayzman *et al.*, in which the correlated hopping of Bi and Ti on split *A* and *B* sites, respectively, is proposed to give rise to a broad distribution of relaxation times [40,41]. Nevertheless, these pictures do not describe how PNRs form, or the dynamic evolution of PNRs with composition and temperature.

Here, in order to better understand the mechanism for PNR formation, we examined the local atomic dynamics near THz frequencies in the weakly coupled relaxor system of Sn-doped $(Ba, Ca)TiO_3$-$x$$BiScO_3$. Recently, it was demonstrated that this material exhibits attractive properties for capacitative energy storage over a broad temperature range from room temperature (RT) to 200 °C [36]. As shown below, small changes in the $BiScO_3$ content significantly change the dielectric and polarization properties of the Sn-doped $(Ba, Ca)TiO_3$-$x$$BiScO_3$ solid solution. Similar results were also reported by Bharadwaja *et al.* for the $BaTiO_3$-$BiScO_3$ solid solution [38]. Separately, the effect of Bi concentration on weakly coupled relaxor behavior was also apparent for a related solid solution of $K_{1-x}Bi_xNb_{1-x}Yb_xO_3$ [42]. These results indicate that incorporation of Bi and Sc has a strong effect on the local dipolar correlations, which is not explained by the existing phenomenological models for weakly coupled relaxors. Rather, we anticipated that addition of $BiScO_3$ could influence the local atomic dynamics and as a consequence the stability of PNRs. To examine the effect of $BiScO_3$ on the local structural dynamics in Sn-doped $(1-x)(Ba, Ca)TiO_3$-$x$$BiScO_3$, we characterized the temporal evolution of the local atomic structure using the method of the dynamic pair distribution function (DyPDF). The evolution of the local structural dynamics in Sn-doped $(Ba, Ca)TiO_3$-$x$$BiScO_3$ is studied as functions of both composition (x) and temperature. The experimental observations suggest that the dynamic stability of local atomic correlations within PNR in this system can be described in terms of ILMs that are created by the addition of Bi at the *A* site, which is similar to the effect of Pb in Pb-based relaxors such as PMN [32]. The random occupancy of the *B* site by Sc^{3+} further disrupts the long-range coupling between the ILMs, thereby preventing long-range structural ordering.

II. EXPERIMENTAL METHOD

Polycrystalline ceramics of compositions $0.05\,BiScO_3$-$0.95\,Ba_{0.78-\delta}Ca_{0.22-\delta}Sn_{2\delta}Ti_{0.96}Sn_{0.04}O_3$ ($\delta = 0.0025$) [$x = 0.05$] and $0.095\,BiScO_3$-$0.905\,Ba_{0.78-\delta}Ca_{0.22-\delta}Sn_{2\delta}Ti_{0.96}Sn_{0.04}O_3$ ($\delta = 0.0025$) [$x = 0.09$] were prepared by using the conventional solid state synthesis route. $BaCO_3$ (Alfa Aesar, 99%), $CaCO_3$ (Sigma-Aldrich, 99%), SnO_2 (UniChem, 99.8%), TiO_2 (Sigma-Aldrich, 99%), Bi_2O_3 (Sigma-Aldrich, 99.99%), and Sc_2O_3 (Sigma-Aldrich, 99.99%) were used as starting materials. The starting materials were mixed in appropriate proportions, ball milled, and subsequently

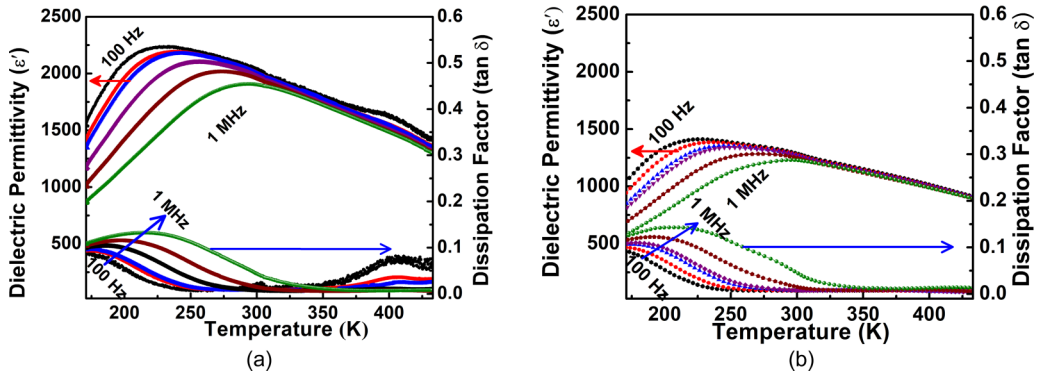

FIG. 1. Temperature-dependent dielectric permittivity and tan δ of Sn-doped $(1-x)$(Ba, Ca)TiO_3-$x$$BiScO_3$ for (a) $x = 0.05$, and (b) $x = 0.09$ ceramics.

calcined to obtain powders of desired compositions. The powders were then pressed in pellet form and sintered at high temperature. Further details for calcination and sintering conditions are provided in Ref. [36].

The sintered pellets were polished and painted with silver electrodes for electrical characterization. An Agilent 4284A Precision LCR meter was used for measurement of temperature- and frequency-dependent dielectric properties. For temperature control, a pour-fill liquid nitrogen cryostat and an electrical furnace were assembled with the LCR meter. A commercial Radiant PE system was used to measure polarization versus electric field hysteresis loops (P-E loops) of the ceramic samples.

For structural characterization, the sintered ceramics were first crushed and sieved to obtain uniformly sized powder samples. The local atomic structure was characterized from the x-ray and neutron total scattering patterns. The high-energy x-ray total scattering patterns were measured at Sector 11-ID-B of the Advanced Photon Source of the Argonne National Laboratory, which provided information of the instantaneous (time-frozen) structure of the materials studied. The inelastic neutron scattering intensities were measured at the ARCS spectrometer of the Spallation Neutron Source of the Oak Ridge National Laboratory, which provided information about the time-dependent evolution of the local structural correlations. The details for analysis of the x-ray and neutron total scattering data are provided in the following section.

III. RESULTS

A. Dielectric and ferroelectric properties

Figure 1(a) shows the temperature-dependent real dielectric permittivity and dissipation factor (tanδ) of $x = 0.05$ ceramic, which are measured with ac fields of frequencies 200 Hz $< f <$ 1 MHz. A broad peak for dielectric permittivity maximum as a function of temperature can be observed. The temperature for maximum dielectric permittivity, or T_m, is a function of frequency and varies from ~200 K at 100 Hz to ~280 K at 1 MHz. These features are characteristic of relaxor ferroelectrics. Figure 1(b) shows the same data for dielectric properties of $x = 0.09$ ceramic [36]. As compared to $x = 0.05$, the dielectric permittivity peak for $x = 0.09$ is broader. For both compositions, deviations from the Curie-Weiss law for ferroelectric phase transition are observed, which indicates local dipole-dipole correlations instead of a long-range ferroelectric state. To gauge the nature of local dipolar correlations, the dielectric permittivity curve above T_m is fitted with the modified Curie-Weiss law, also known as the Uchino and Nomura formula [43]:

$$\frac{1}{\varepsilon} - \frac{1}{\varepsilon_m} = \frac{(T - T_m)^\gamma}{C}, \tag{1}$$

where ε_m is the dielectric permittivity value at T_m, and C is a constant and γ is the critical exponent. The value of γ is ~1 for an ideal ferroelectric, whereas the same is higher for relaxors. For purely zero-point quantum fluctuations $\gamma \sim 2$. For relaxors, γ typically lies between 1 and 2 [43,44]. The γ values obtained from the fitting analysis are 1.59 ± 0.02 and 1.71 ± 0.02 for $x = 0.05$ and $x = 0.09$, respectively, which indicates the existence of relaxor behavior and that the dipolar correlations are rather weak. (See Fig. S1 in the Supplemental Material for details [45]. Also see [46–49].)

Beside the Uchino-Nomura criterion, we also employed the dynamic scaling relation based on the Vogel-Fulcher law to characterize the relaxation properties of the local dipoles [50,51]. The Vogel-Fulcher law is widely used to characterize the frequency dispersion of dielectric relaxation in materials with short-range dipolar correlations [4,11], and can be represented as

$$\omega = \omega_o \exp\left[\frac{-E_a}{k_B(T_m - T_f)}\right], \tag{2}$$

where E_a is the activation energy, $\omega_o = 2\pi f_o$, f_o is known as the attempt frequency (it corresponds to the Debye relaxation frequency), T_m is the temperature of the maximum permittivity, T_f is the freezing temperature, and k_B is the Boltzmann constant. The fitting analysis yielded the following parameters, $f_o = 7.2 \times 10^{10}$ Hz and 4.1×10^{11} Hz, $T_f = 130.8$ K and 93.1 K, and $E_a = 0.08$ eV and 0.12 eV for $x = 0.05$ and $x = 0.09$, respectively. The attempt frequencies (f_o) and activation energies (E_a) of the current samples are in the same range as that of weakly coupled relaxor ferroelectrics [34]. The high activation energies signified that the neighboring clusters are weakly coupled.

The polarization-electric field (P-E) hysteresis loops at selected temperatures for $x = 0.05$ and $x = 0.09$ are depicted in Fig. 2. There is a clear difference in the temperature-dependent polarization behavior of the two materials. At

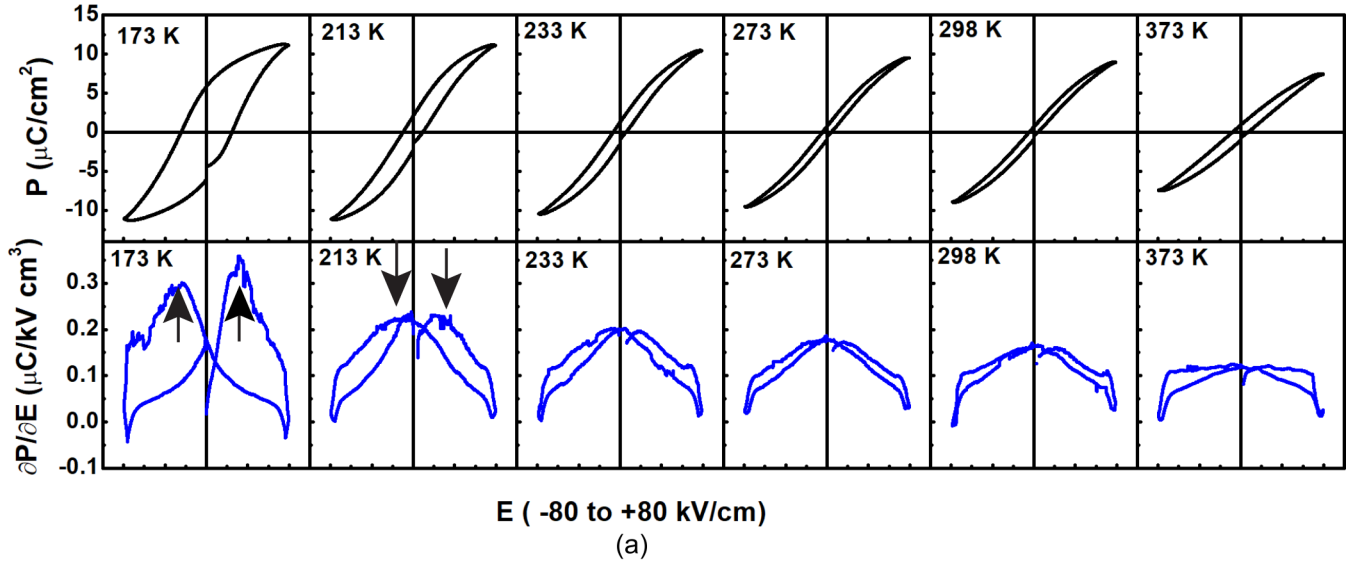

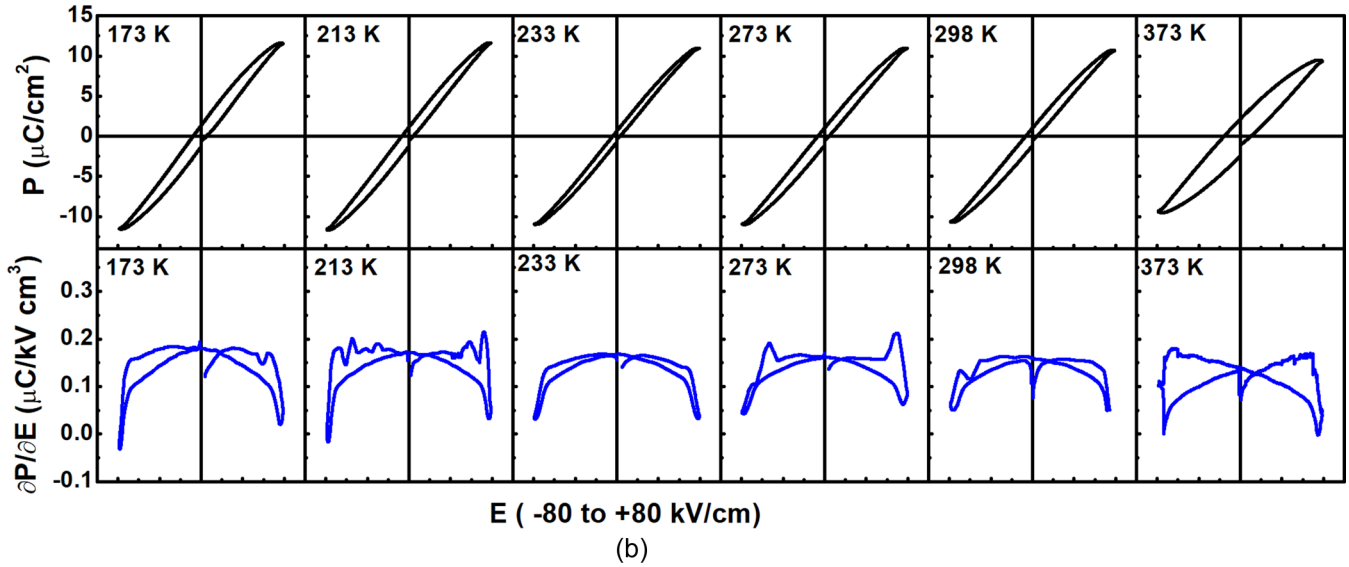

FIG. 2. Temperature-dependent *P-E* hysteresis loops and their corresponding derivative curves ($\partial P/\partial E$ versus E) of Sn-doped $(1-x)$(Ba, Ca)TiO_3-$x$$BiScO_3$ for (a) $x = 0.05$, and (b) $x = 0.09$ ceramics.

temperature $T = 173$ K, the *P-E* loop for $x = 0.05$ exhibits a characteristic that is typical of polarization switching; that is, the curves for increasing/decreasing electric fields are strongly nonlinear and there is a large remanent polarization at zero field. However, the *P-E* loops become progressively thinner and linear with increase in temperature. In contrast, for $x = 0.09$, the *P-E* loops remain nearly linear at all measurement temperatures, with no significant remanent polarization. In order to further ascertain the presence, or otherwise, of ferroelectric switching, the $\partial P/\partial E$ versus E curves are extracted for each measurement temperature, which are shown below the corresponding *P-E* loops. For a linear *P-E* curve, $\partial P/\partial E$ should remain constant with E. For a nonlinear polarization behavior, $\partial P/\partial E$ should decrease with E, but should not show an inflection point at an intermediate field. In the case of ferroelectric switching, the $\partial P/\partial E$ versus E curve will exhibit an inflection point at coercive field or E_c, such as observed for $x = 0.05$ at $T = 173$ K (indicated by arrows in Fig. 2). For a purely lossy dielectric, the $\partial P/\partial E$ curve is expected to appear as a cross, such as observed for $x = 0.09$ at $T = 373$ K. It can be observed that while at $T = 173$ K, the $x = 0.05$ ceramic shows clear indication of ferroelectric switching with inflection points in $\partial P/\partial E$, the signal for the same becomes progressively weaker as the temperature is increased. Based on this, it can be ascertained that for $x = 0.05$, the material transforms from a high-temperature paraelectric phase to a polar phase with decreasing temperature, although such a transition occurs over a broad temperature from 298 to 173 K. For $x = 0.09$, there is no obvious indication of an inflection point in the $\partial P/\partial E$ curve at any measurement temperature, indicating no transition to a macroscopic polar state occurs at lower temperatures.

B. Local atomic structure using pair distribution function analysis

For relaxors, local deviations from the spatially averaged crystal structure give rise to their attractive dielectric and other functional properties [4,11]. These local ionic displacements are, however, correlated over nanometer lengths, and therefore when averaged over longer length scales the net ionic displacements amount to either zero or a very small value. As a consequence of this, these ionic displacements are not measured from Rietveld refinement against x-ray/neutron Bragg diffraction peaks, which instead inform only about the spatially averaged crystal structure [52]. In comparison, the locally correlated atomic arrangements can be better characterized using pair distribution function (PDF) analysis of x-ray/neutron total scattering patterns.

1. Instantaneous local structure

The pair distribution function (PDF) represents pairwise atomic correlations as a function of interatomic distances r. The PDF $G(r)$ is obtained from the total scattering pattern using the relation

$$G(r) = \frac{2}{\pi}\int_{Q_{\min}}^{Q_{\max}} Q[S(Q)-1]\sin QrdQ, \qquad (3)$$

where Q is the scattering vector, $S(Q)$ is the total scattering structure factor, and r represents the interatomic distances [53]. In this treatment, since no implicit assumption of translational symmetry is made, the obtained pairwise atomic correlation is sensitive to structural distortions present over multiple length scales. The PDF technique, therefore, is a powerful method to characterize the locally correlated interatomic correlations within the PNRs. Here, an important clarification is in order. Conventionally, the total scattering measurements are made with no distinction between different energy transfers. In other words, the scattering intensity or $S(Q)$ is integrated over all energy transfers. Consequently, provided that the energy integration is done over a large enough energy range, such as implemented in a high-energy synchrotron x-ray scattering experiment, the $G(r)$ obtained from Fourier transform of the energy integrated $S(Q)$ represents the same-time correlations or an instantaneous snapshot of the local atomic structure [53].

Figure 3 compares the x-ray PDFs of powdered ceramics of $x = 0.05$ and $x = 0.09$ compositions at temperature $T = 280$ K. The PDFs are shown for $r < 6$ Å, which represent the nearest and next-nearest atomic neighbors. The two patterns appear virtually indistinguishable from each other. The x-ray PDFs for $x = 0.05$ and $x = 0.09$ at 280 K were fitted using PDFGUI in the range of $r < 10$ Å [54], using three different structures, viz., rhombohedral ($R3m$), orthorhombic ($Amm2$), and tetragonal ($P4mm$). The best fit is obtained for the orthorhombic structure ($R_w \sim 6.8\%$), as compared to the rhombohedral ($R_w \sim 10.8\%$) and tetragonal ($R_w \sim 11.9\%$) structures, as shown in Fig. 4. Similar values for R_w for the three different phases were obtained for $x = 0.09$ composition (see Fig. S2 in the Supplemental Material [45]; also see [49]). However, it is also noted that the TiO_3 octahedron is highly distorted in the orthorhombic phase, which gives rise to a bond valence sum (BVS) of 3.18 for Ba^{2+} and 3.52 for Ti^{4+},

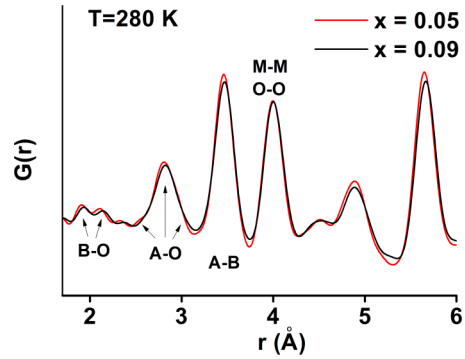

FIG. 3. (a) Comparison of the instantaneous local structure of Sn-doped $(1-x)$(Ba, Ca)TiO_3-$x$$BiScO_3$, for $x = 0.05$ and $x = 0.09$ compositions.

indicating that Ba^{2+} is severely overbonded, while Ti^{4+} is underbonded. In comparison, for the rhombohedral structure, the calculated BVSs are 2.79 for Ba^{2+} and 3.83 for Ti^{4+}. For the tetragonal structure, the calculated BVSs are 2.81 for Ba^{2+} and 3.73 for Ti^{4+}. Therefore, rhombohedral/tetragonal appears as a more plausible model for the instantaneous local atomic structure, as compared to the orthorhombic structure.

Figure 5 shows the temperature-dependent evolution of the PDFs for the two compositions from 80 to 400 K. The peaks in the PDF for $x = 0.09$ are slightly broader as compared to those for $x = 0.05$, especially at higher temperatures. Nevertheless, very little difference can be noted between the PDFs of the two compositions. The above results indicate that there are minimal changes in the local instantaneous structure, either as a function of composition or temperature, which are covered in this study. This is remarkable given that the macroscopic dielectric and polarization properties evolve quite significantly over the same temperature and composition ranges, as described in the previous section.

2. Time-dependent local structure

The above example illustrates that the instantaneous snapshot of the local atomic structure is insufficient in addressing the relationship between local atomic structure and macroscopic properties of weakly coupled relaxors. Specifically, the conventional PDF does not inform about the *timescale* over which the local atomic correlations vary. Since the PNRs are intrinsically dynamic in nature, information about the time-dependent evolution of their atomic structure becomes necessary in order to better comprehend formation of PNRs.

Recent works have shown that the dynamic changes in the local atomic correlations can be characterized using a dynamic PDF (DyPDF) method [32,33]. In this method, the dynamic structure factor $S(Q, E)$, where $E = h\nu$ is the energy transfer, is obtained from the energy resolved total scattering intensity $I(Q, E)$ after implementing background correction and normalization, such as described in Refs. [32,33]. Fourier transformation of $S(Q, E)$ from Q to r yields the DyPDF, or $G(r, E)$, which represents pairwise atomic correlations for interatomic distances r and excitation energy E. In other words, $G(r, E)$ represents the pairwise atomic correlations that are stable with the characteristic frequency, $\nu = E/h$, where h

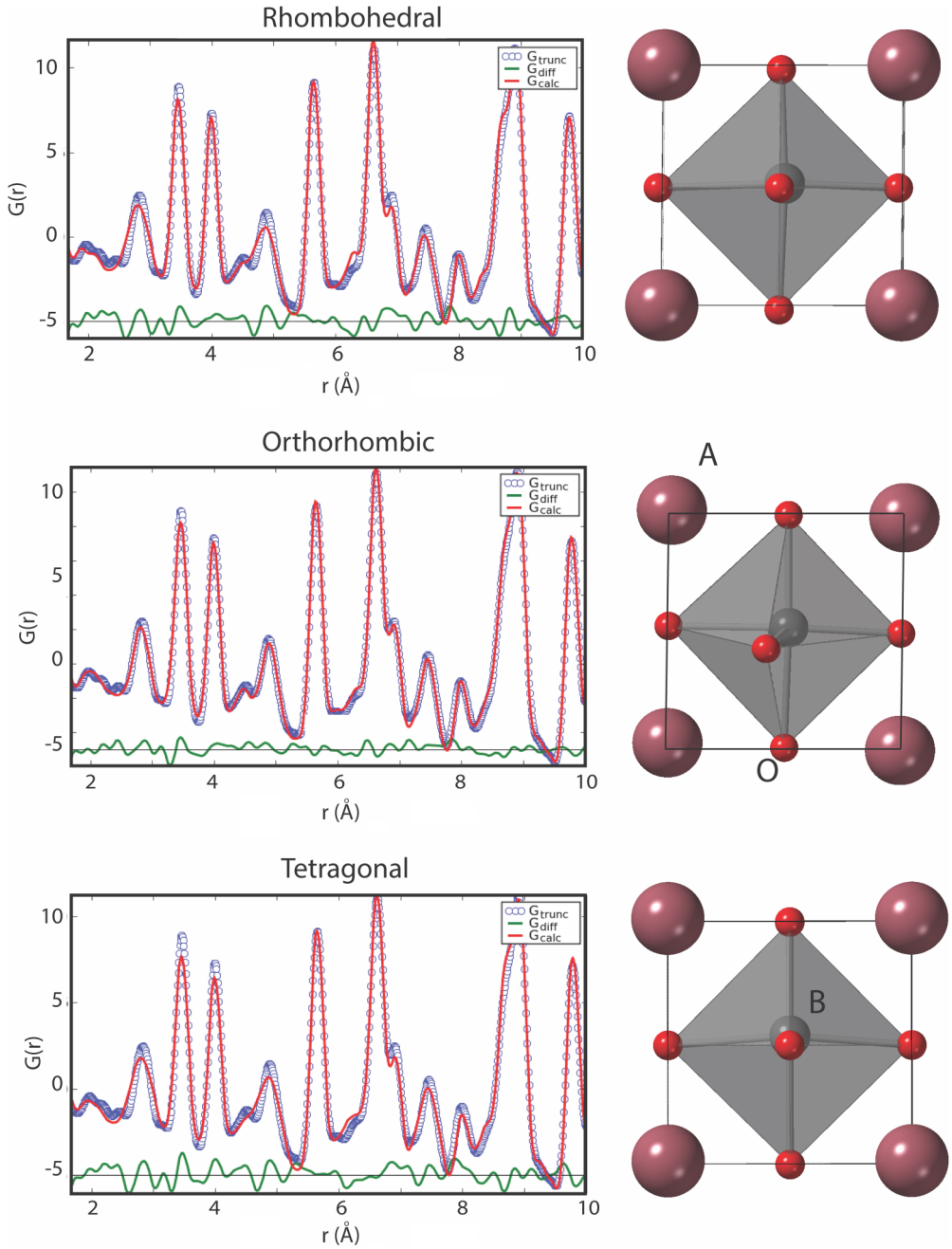

FIG. 4. Fits of the instantaneous x-ray PDFs of Sn-doped $(1-x)$(Ba, Ca)TiO_3-$x$$BiScO_3$, for $x = 0.05$, using three different structural models, viz., rhombohedral, orthorhombic, and tetragonal. The lines mark the unit cell for the pseudocubic unit cell.

is the Planck's constant. In the conventional PDF, the total scattering factor is integrated over all energy transfers, that is, $S(Q) = \int S(Q, E)dE$, and therefore the corresponding $G(r)$ provides the same-time atomic correlations or instantaneous snapshots of the structure. For the ideally elastic scattering intensity or $E = 0$, Fourier transformation of $S(Q, E = 0)$ yields the *time-averaged* pairwise atomic correlations. For obtaining atomic correlations over an intermediate time period of $t = 1/\nu = h/E$, Fourier transformation needs to be performed for the dynamic scattering factor integrated over a small range of energy transfer. This is implemented by evaluating $S_{\text{meas}}(Q, E) = \int w(E-E')S(Q, E')dE'$, where $w(E - E')$ is the energy resolution function of the instrument. The measurement conditions and data analysis methods, viz., the incident energy used at ARCS, background subtraction, and the energy integration window, were the same as described in Ref. [33]. The methodology described in Ref. [33] provides adequate resolution for $G(r, E)$ in the ranges of $r \sim 3-4.5$ Å and $E \sim 3.4$–9.5 meV, which are of primary interest here.

Figures 6(a)–6(d) compare the $G(r, E)$ of the two compositions for different energy transfers E, or corresponding frequencies, $\nu = E/h$, at temperature $T = 270$ K. Figure 6(a) shows the time-averaged $(E = 0)$ atomic correlations for the two compositions, which appear to be virtually the same. The interatomic distances as noted from the x-ray PDF are marked for reference. A clear difference can be noted between the

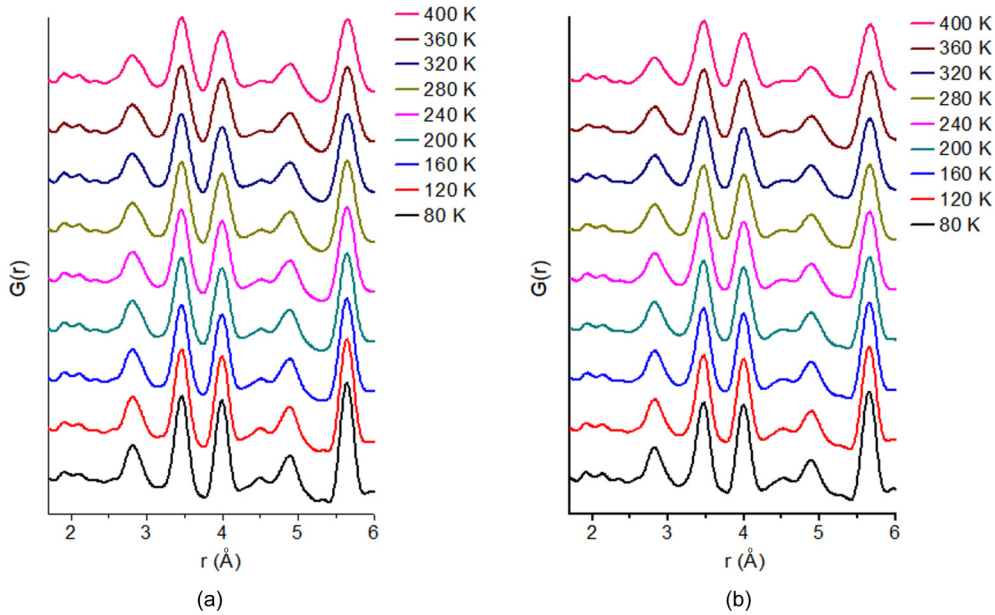

FIG. 5. Temperature-dependent x-ray PDFs of Sn-doped $(1-x)$(Ba, Ca)TiO_3-$x$$BiScO_3$, for (a) $x = 0.05$ and (b) $x = 0.09$.

time-averaged and frequency-limited G(r, E) for $r \sim 3$–4.5 Å. In the instantaneous x-ray PDF (Fig. 3), a well-defined split is noted between the peaks at $r \sim 3.5$ Å and at $r \sim 4$ Å. In contrast, for the time-averaged PDF, the peak appears asymmetric without a clear split. For sufficiently faster timescales, such as 2.3 THz, which is represented by $G(r, E = 9.5\,\text{meV})$, the split between the peaks at $r \sim 3.5$ Å and $r \sim 4$ Å becomes clear. In order to characterize the temporal change in the local atomic structure, we next compared the experimental DyPDF with the calculated neutron PDF peak profiles for 3.5 Å $< r <$ 4.5 Å. Figures 6(e) and 6(f) show the calculated neutron PDF peak profiles for the two plausible structures, viz., tetragonal and rhombohedral. The neutron PDFs are calculated based on the refined structures obtained from fitting of the corresponding x-ray PDFs (Fig. 4). It is clear that the peak between 3.5 and 4.5 Å is split for the rhombohedral structure, but only a broad asymmetry is observed for the tetragonal structure. By comparing the DyPDF patterns with the calculated neutron G(r) peak profiles, it can be ascertained that the instantaneous structure is closer to rhombohedral, while the time-averaged structure is closer to tetragonal. A gradual transition from rhombohedral to tetragonal structure occurs with longer timescales.

The above situation can be compared to the order-disorder model for $BaTiO_3$, as described by Comes *et al.* [55,56]. In the order-disorder model, the local atomic structure is rhombohedral with Ti displaced along the ⟨111⟩ directions. However, the average structure can be different depending on the ordering of individual Ti displacements. At low temperatures below 183 K, the ⟨111⟩ Ti displacements are ordered over a longer range along one-dimensional chains, which gives rise to an average rhombohedral phase. In comparison, a disordering of the Ti displacements among four of the possible eight ⟨111⟩ directions at high temperatures (>283 K) gives rise to an average tetragonal phase. A similar progression from rhombohedral to tetragonal structure is observed here with progression of time. In DyPDF the local atomic correlations are sharply defined at energies for which the corresponding frequency, $\nu = E/h$, is above the frequency of the fluctuating atomic displacements. At fast timescales, such as 2.3 Hz, the local atomic correlations are closer to a rhombohedral structure, which has B-site atoms displaced along ⟨111⟩. On the other hand, if the measurement frequency for DyPDF, $\nu = E/h$, is lower than that of the frequency of the atomic displacements, the fluctuating atomic displacements are averaged over a given time period. This results in the appearance of a tetragonal structure over longer timescales, such as observed here for 0.8 THz or the time-averaged structure.

A difference in the local atomic correlations for the two compositions becomes obvious at intermediate timescales. For $E = 4.9$ meV or $\nu = 1.2$ THz, the split between the peaks at $r \sim 3.5$ Å and $r \sim 4.5$ Å is clear for $x = 0.05$, but only a broad asymmetric peak is observed for $x = 0.09$. For $E = 9.5$ meV or $\nu = 2.3$ THz, the $G(r, E)$ for the two compositions approach each other. In other words, the effect of composition on the A-B interatomic correlations is dependent on the timescale over which they are observed. This also indicates that the local atomic correlations in these compounds are not "static" [40,41], but rather follow a dynamic evolution. For example, at $T = 270$ K and for $x = 0.05$, the local atomic correlations in the rhombohedral structure stay stable for frequencies as low as 1.2 THz. In contrast, for $x = 0.09$, a structural transition resembling rhombohedral to tetragonal is observed at 1.2 THz, indicating that the local atomic correlations do not remain stable at this frequency. The difference in G(r, E) for the two compositions near 1 THz can explain their temperature-dependent polarization behavior, as shown in Fig. 2. From Fig. 2, it can be observed that ferroelectric switching is more obvious for $x = 0.05$ below 270 K, as compared to $x = 0.09$. If the local atomic correlations are stabilized near 1 THz or the transverse optic (TO) phonon frequencies, this gives rise to PNRs with slower dynamics, and therefore transition to a polar phase can be expected.

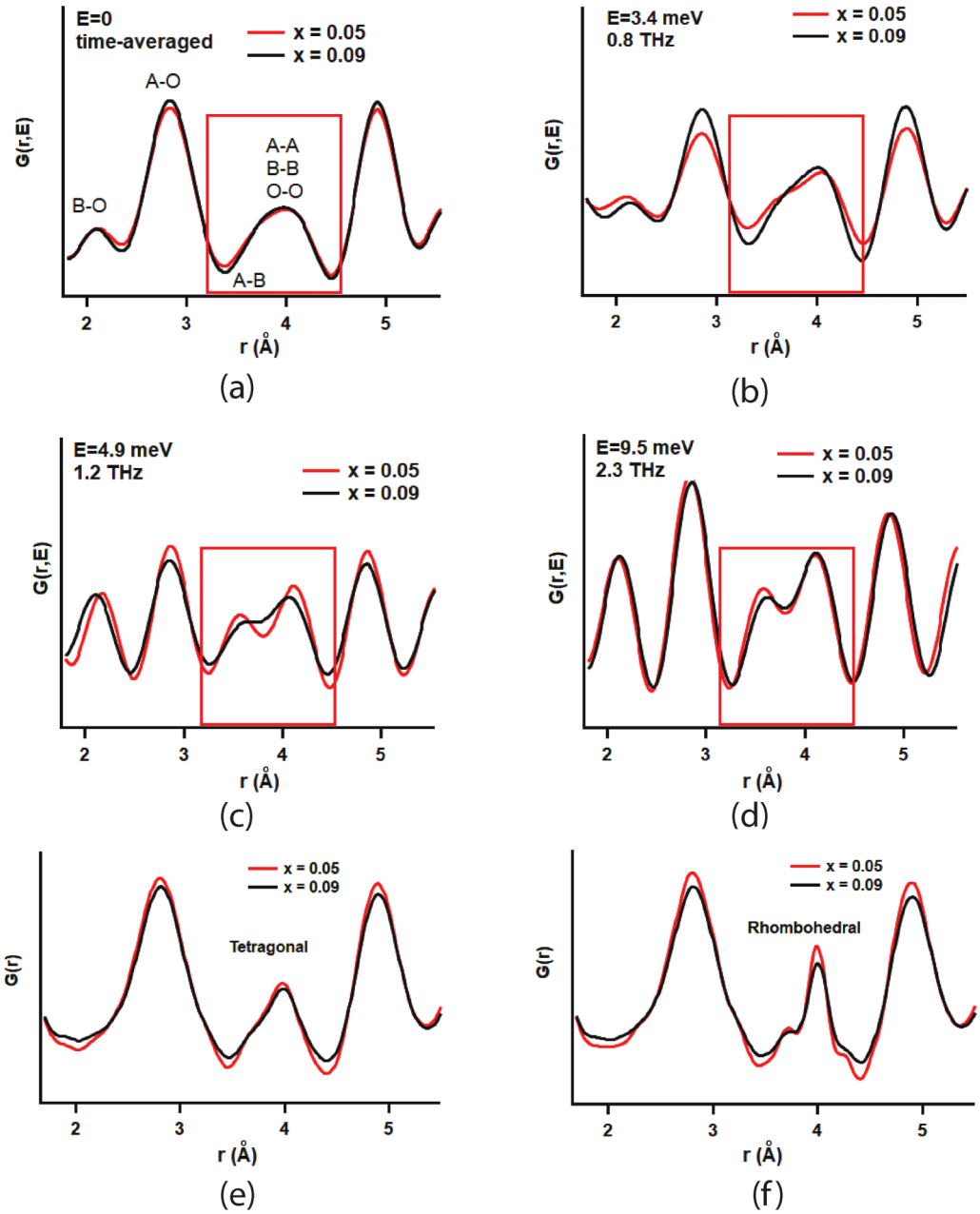

FIG. 6. (a)–(d) Comparison of the neutron DyPDFs for $x = 0.05$ and $x = 0.09$ at various energy transfers, or measurement frequencies, for temperature $T = 270$ K. The instantaneous interatomic distances, as observed in the x-ray PDFs (a), are marked for reference. (e), (f) The calculated neutron G(r) profiles for the tetragonal/rhombohedral structures, which are obtained from refinement of the x-ray PDFs.

Figure 7(a) shows the evolution of DyPDFs for the two compositions as a function of temperature. The primary interest is for the region $r \sim 3$–4.5 Å, which features *A*-*B*, *M*-*M*, and *O*-*O* correlations and for which a clear difference between the two compositions is observed in the DyPDF. As noted above, at $T = 270$ K and $E = 4.9$ meV, the peaks at $r \sim 3.5$ Å and $r \sim 4$ Å are split for $x = 0.05$, but not for $x = 0.09$. The same information is apparent from the circled regions of the two-dimensional (2D) plots for $G(r, E)$ at $T = 270$ K. Figure 7(b) shows the temperature-dependent G(r, E) line profiles for the two compositions for 3 Å $< r <$ 4.5 Å. For $x = 0.05$, the split between the peaks at $r \sim 3.5$ Å and $r \sim 4$ Å is more clearly resolved for $E = 4.9$ meV (or $\nu = 1.2$ THz) at $T = 270$ K, indicating stabilization of the rhombohedral structure with ⟨111⟩ *B*-atom displacements. In contrast, for composition $x = 0.09$, there is a weak shoulder present at $r \sim 3.5$ Å in the DyPDF for $\nu = 1.2$ THz at all temperatures above 270 K, which indicates that the instantaneous rhombohedral structure is not stable beyond 1.2 THz for temperatures 270 K and above. This correlates well with the observed differences in dielectric permittivity spectra of the two compositions. For $x = 0.05$, a comparatively stronger peak is observed for the weak-field dielectric permittivity at $T = 270$ K measured for applied electric fields of frequency 1 MHz (see Fig. 1), which results from stronger coupling between PNRs that are more stable. In comparison, a much broader dielectric spectrum

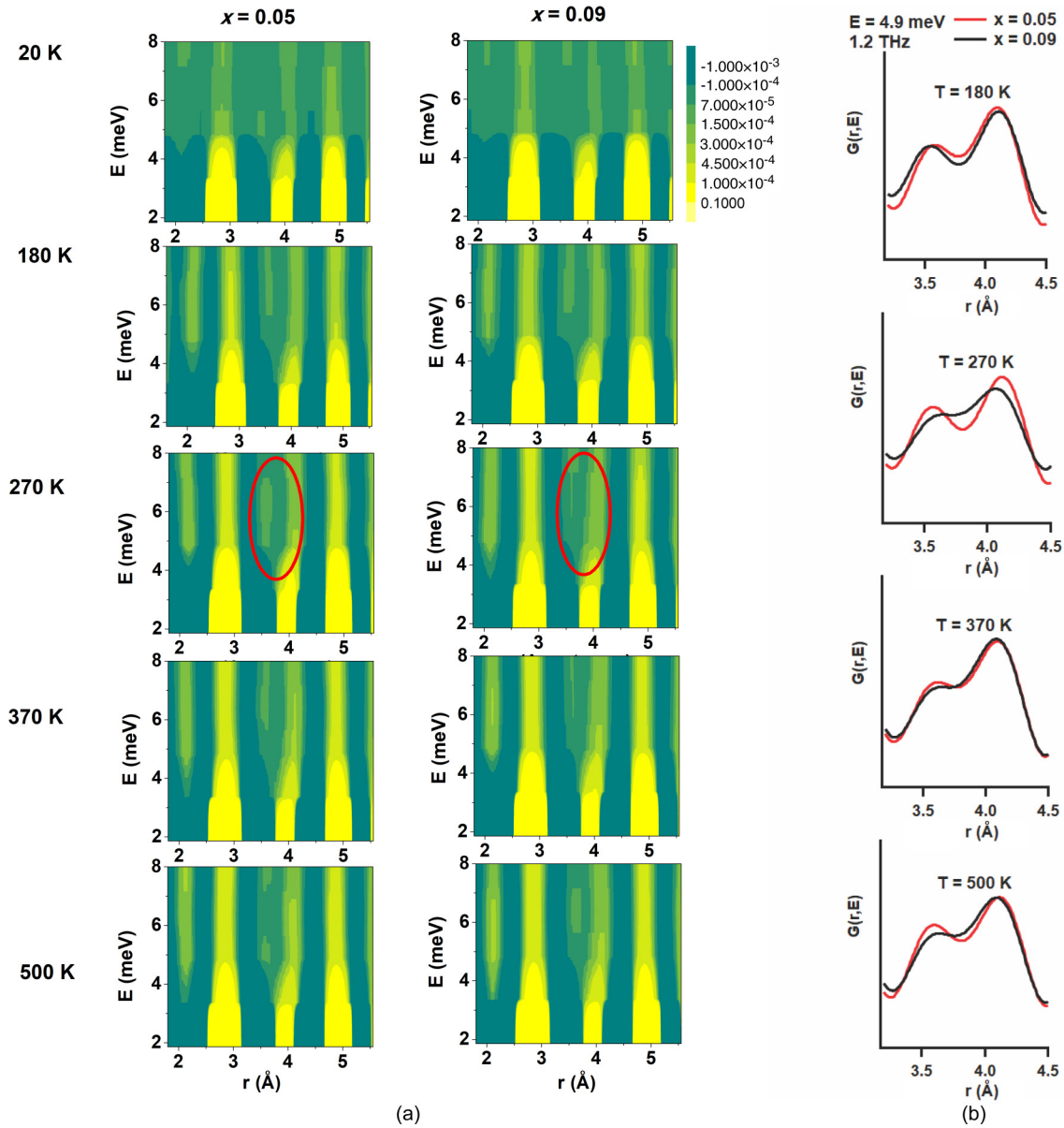

FIG. 7. (a) Composite $G(r, E)$ patterns for $x = 0.05$ and $x = 0.09$ at different measurement temperatures. The most notable difference in the $G(r, E)$ of the two compositions can be observed near the circled region. (b) $G(r, E)$ line profiles in the region 3 Å $< r <$ 4.5 Å, for $x = 0.05$ and $x = 0.09$, at different measurement temperatures.

is observed for $x = 0.09$ (see Fig. 1), which is reflective of weak coupling between the PNRs due to their greater dynamic fluctuations.

IV. DISCUSSION

The results presented above reveal the critical effect of $BiScO_3$ concentration on the local atomic dynamics, and the consequent dielectric and ferroelectric properties, of Sn-doped $BaTiO_3$-$BiScO_3$ solid solution. Based on analysis of low-field dielectric permittivity, the system can be classified as a weakly coupled relaxor, which is characterized by a broad dielectric spectrum and a relatively higher E_a, as compared to traditional relaxors. With increasing Bi and Sc substitutions, at A and B sites, respectively, the dielectric spectrum becomes broader and E_a increases, which indicates increasing restriction towards long-range dipole ordering. Additionally, transition to a low-temperature polar phase is more clearly observed for a lower Bi/Sc content ($x = 0.05$). In previous works, these characteristics were attributed to a weak coupling between nanoscale polar clusters that form upon Bi/Sc substitutions [34,35]. However, direct evidence of the effect of $BiScO_3$ concentration on nanoscale polar correlations has been absent.

To elucidate the local atomic correlations, we undertook PDF measurements of Sn-doped (Ba, Ca)TiO_3-$BiScO_3$ as a function of temperature. The instantaneous pairwise atomic correlations, as obtained from x-ray total scattering, did not show any significant change as a function of either composition or temperature. However, we noticed a significant difference in the short-range atomic correlations, when such correlations are evaluated over different timescales as revealed

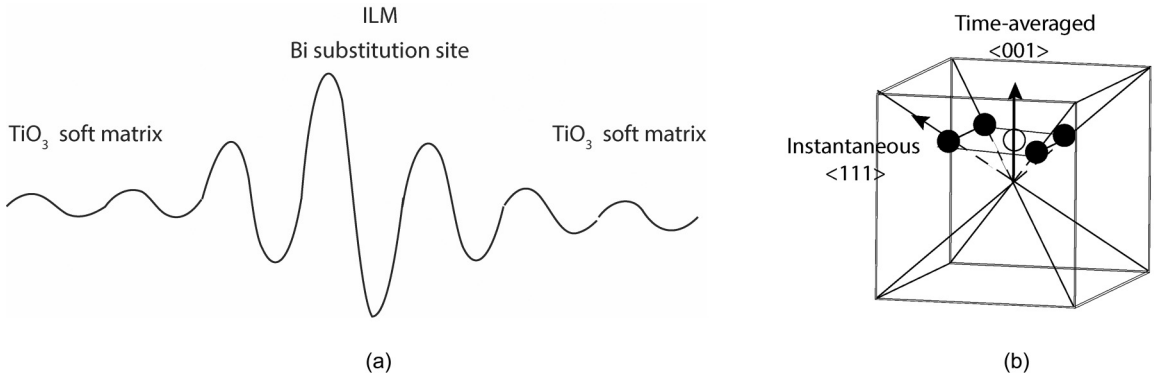

FIG. 8. (a) Illustration of the ILM model, which depicts substitution sites in a dielectrically soft matrix. (b) Schematic of *B*-site atomic displacements for the instantaneous and the time-averaged structures.

by the neutron DyPDF. Notably, for both the compositions and for temperatures RT and above, the DyPDF indicates that ⟨111⟩-type *B*-site atomic displacements in the rhombohedral structure do not remain stable for sub-THz frequencies. In other words, the PNRs are not visible below THz frequencies, because they are dynamic. This is in contrast to the "static" (stable below THz frequencies) PNRs reported for the related ferroelectric relaxor $Ba(Zr, Ti)O_3$ [33]. The weak coupling between PNRs in $BaTiO_3$-$BiMeO_3$ systems, as described in earlier works [34,35], can therefore be described as a secondary effect of greater dynamic fluctuations of the same in the time domain.

Changes in the dynamic short-range atomic correlations can be interpreted based on the model of intrinsic local modes (ILMs) or discrete breathers, which was described earlier for the Pb-based relaxor PMN [29]. ILMs are bound states of elementary polar excitations, which are embedded in a soft dielectric matrix. In PMN, the ILMs are constituted by local off-centered displacements of Pb in the oxygen cage [57], while $(Mg/Nb)O_3$ constitutes the soft dielectric matrix. The off-centered displacement of Pb^{2+} is caused by the presence of lone pair electrons in the outermost 6*s* orbital. Similar to Pb^{2+}, Bi^{3+} has a lone pair of electrons in the outermost 6*s* orbital, which incentivize the off-centered displacement of Bi in the oxygen cage, such as those described in Refs. [41,58]. The local modes caused by Bi substitution sites constitute ILMs in the $(Ba, Ca)TiO_3$-$BiScO_3$ solid solution. In analogy with PMN, TiO_3 provides the soft dielectric matrix in the $(Ba, Ca)TiO_3$-$BiScO_3$ lattice. Furthermore, the random occupancy of the *B* site by Sc^{3+} ions disrupts the coupling between the ILMs, giving rise to regions with short-range dipolar correlations or PNRs. The microscopic picture is schematically illustrated in Fig. 8(a). Here, for the present composition, additional roles are also possibly played by Ca and Sn substitutions. As described in Ref. [29], the Ti ions in the vicinity of Ca constitute secondary ILMs, in addition to the Bi^{3+} ions. Furthermore, Sn^{2+} present at the *A* site (see Fig. S3 in the Supplemental Material [45]) plays a similar role to that of Pb^{2+} due to the presence of lone-pair electrons [59] and therefore constitutes additional ILMs. However, the primary concern in the present study involves the effect of Bi/Sc substitutions, which is implemented through systematic variation in $BiScO_3$ content.

In the two extreme scenarios described in Refs. [29,30], the dilute and dense distributions of ILMs can lead to distinct dynamic polarization characteristics. In the dilute case, the ILM energy lies below the TO frequencies, which leaves an energy window into which the TO mode can soften and therefore enables the system to transition to a ferroelectric-type polar state. This is observed, for example, in $(Sr_{1-1.5x}Bi_x)TiO_3$, for $x < 0.0267$ [60]. In contrast, for dense distribution of ILMs, the ILMs occupy a broader energy window, which hinders a softening of the TO mode and therefore the transition to a ferroelectric-type uniform polar state is prohibited, an example for which is PMN. The present case should correspond to the dilute limit. Within this limit, a broad transformation is possible for the Sn-doped $(Ba, Ca)TiO_3$-$BiScO_3$ solid-solution system depending on dopant content. For a relatively lower Bi content, that is, $x = 0.05$, we observe a weak dielectric permittivity peak and clear transition to a ferroelectric-type hysteresis at a lower temperature of 173 K. In comparison, for a higher Bi content for $x = 0.09$, the dielectric permittivity peak is much broader and no significant indication of polarization switching is noted at any measured temperature.

In correlation to the composition-dependent dielectric and polarization properties, we also observed from DyPDF the effect of ILM concentration on the temporal short-range atomic correlations. In undoped $BaTiO_3$, the energy of the TO soft mode at the zone center for the TiO_3 matrix lies at ∼2.5–4.5 meV or 0.6–0.8 THz (300–420 K) [61,62]. In Sn-doped $(Ba, Ca)TiO_3$-$BiScO_3$, if an energy window is left for the TO mode to soften, it would allow for resonance between the TO mode and the ILMs, leading to stronger dipolar correlations at lower frequencies. As can be observed from the DyPDF, for low Bi concentration, i.e., $x = 0.05$, the rhombohedral structure remains stable to at least 1.2 THz, which indicates stronger correlations for the ⟨111⟩-type *B*-site displacements. With increasing Bi doping, Bi ions have more Bi ions in the neighborhood to form dynamic ILM centers. Because Bi in $BiScO_3$ shows antiparallel shifts from high-symmetry positions [63,64], the Bi-Bi interaction in the background of ferroelectric $(Ba, Ca)TiO_3$ would increase the ILM frequency, eventually above 1 THz. This would result in weaker resonance between the ILMs and the soft TO mode as predicted from the ILM model. As a result, for $x = 0.09$, the ⟨111⟩-type *B*-site displacements are disordered near THz frequencies.

An averaging of the disordered ⟨111⟩ atomic displacements would give the appearance of a tetragonal structure, such as schematically illustrated in Fig. 8(b). Note that this view is consistent with earlier measurements, which indicated tunneling or hopping motion of Ti between several disordered states in $BaTiO_3$ near THz frequencies [65,66].

The frequency for thermal fluctuations of PNRs in the compounds of the current study are likely of the order of MHz, as indicated in the peak frequencies of dielectric permittivity. The prevalent view has been that Bi simply breaks up ferroelectric correlation in the matrix, dividing the system into nanoscale domains [35,54]. However, the present result reveals a more active, dynamic role of Bi. Note that in the above description of PNRs based on ILMs, we do not explicitly ascertain the PNRs to be static regions with correlated polarization. Rather, the doping sites act as ILMs around which regions with correlated polarization dynamically form and fluctuate with frequencies of the order of THz. For longer timescales (or lower frequencies), these correlations decay due to relaxation of the local dipoles of PNRs. Earlier studies using neutron backscattering and neutron spin-echo measurements indicated such slower relaxation of PNRs at GHz frequencies [24–26], but they do not necessarily inform about how PNRs form.

The stability of the locally correlated regions is the main determining factor for transition to a ferroelectric-type polar state at lower temperatures. For ferroelectric relaxors, the local correlations within the PNRs remain below THz frequencies at low temperatures, such as shown for $Ba(Zr_xTi_{1-x})O_3$ in Ref. [33]. Weakly coupled relaxors show behavior intermediate between dipolar glasses and relaxor ferroelectrics in the sense that the frequencies of the atomic fluctuations within the PNRs remain just near ∼1 THz, which is further subject to compositional and temperature changes.

Another interesting possible consequence of the ILM model could be the reentrant phenomena in weakly correlated relaxors. At lower temperatures, as the TO mode hardens, it should lead to a widening in the gap between the ILMs and the TO mode, leading to weaker resonance between them and resultant weaker local dipolar correlations. A consequence of this is that the overall macroscopic polarization will decrease with decrease in temperature. This is indeed observed for $BaTiO_3$-$BiScO_3$ ceramics, which is described as a reentrant phenomenon [39]. The current DyPDF measurements indicate that the local correlations for shorter *A*-*B* bond distances become weaker at lower temperatures [see Fig. 7(a) for $T = 20$ K], which would be consistent with this view. However, further investigation with more detailed DyPDF measurement at intermediate temperature steps will be necessary to correlate reentrant phenomena in weakly coupled relaxors to dynamic atomic correlations.

V. CONCLUSION

In summary, we have investigated the dynamic atomistic origin of PNR formation leading to weakly coupled relaxor behavior in Sn-doped $(1-x)(Ba, Ca)TiO_3$-$xBiScO_3$, based on macroscopic polarization, x-ray PDF, and neutron DyPDF measurements. The material exhibits a frequency-dispersive broad dielectric permittivity peak and high activation energy for dipolar relaxations, which are characteristics of weakly coupled relaxors. In addition, transition to a low-temperature polar phase strongly depends on the concentration of $BiScO_3$ or x. Analysis of the x-ray snapshot PDF indicated no significant changes in the instantaneous local structural correlations with either composition or temperature in the range from 400 to 80 K. However, neutron DyPDF indicated changes in the dynamics of local atomic correlations near THz frequencies as a function of both composition and temperature. It is noted for this system that the instantaneous local atomic correlations do not remain stable at sub-THz frequencies, which results in less stable PNRs and therefore can explain their weakly coupled relaxor behavior. Furthermore, for timescales near 1 THz, the stability of the local atomic correlations remains stronger for lower Bi/Sc content, which indicates the effect of composition on material properties. The results are interpreted in terms of ILMs, which are mainly introduced through substitution of Bi at the *A* site. Based on the current findings, it is proposed that investigation of the dynamics of local atomic correlations, rather than instantaneous structural snapshots, is critical for understanding the microscopic origins of relaxor behavior.

ACKNOWLEDGMENTS

A.P. gratefully acknowledges funding support from CityU (Projects No. 7004967 and No. 9610377) and EDGE (Project No. 6000688). T.E. and W.D. were supported by the US Department of Energy, Office of Science, Basic Energy Sciences, Materials Sciences and Engineering Division. F.M. and M.R.V.J. gratefully acknowledge the support by the Danish National Research Foundation (DNRF93) and the Danish Agency for Science, Technology and Innovation (DANSCATT). Affiliation with the Center for Integrated Materials Research (iMAT) at Aarhus University is gratefully acknowledged. A portion of this research used resources at the Spallation Neutron Source, a DOE Office of Science User Facility operated by the Oak Ridge National Laboratory. This research used resources of the Advanced Photon Source, a US Department of Energy (DOE) Office of Science User Facility operated for the DOE Office of Science by Argonne National Laboratory under Contract No. DE-AC02-06CH11357. The authors gratefully acknowledge technical assistance from Hui Wang and Zengquan Wang for neutron scattering measurements at ORNL. A.P. and S.N. acknowledge technical support from Daniel Yau at City University of Hong Kong.

[1] G. H. Haertling, Ferroelectric ceramics: History and technology, J. Am. Ceram. Soc. **82**, 797 (1999).

[2] L. E. Cross, Relaxor ferroelectrics, Ferroelectrics **76**, 241 (1987).

[3] G. A. Smolenskii, V. A. Isupov, A. I. Agranovskaya, and S. N. Popov, Ferroelectrics with diffuse phase transitions, Sov Phys. Solid State **2**, 2584 (1961).

[4] A. A. Bokov and Z. G. Ye, Recent progress in relaxor ferroelectrics with perovskite structure, J. Mater. Sci. **41**, 31 (2006).

[5] W. Kleemann, Random fields in relaxor ferroelectrics—a jubilee review, J Adv. Dielectr. **02**, 1241001 (2012).

[6] G. A. Samara, The relaxational properties of compositionally disordered ABO_3 perovskites, J. Phys.: Condens. Matter **15**, R367 (2003).

[7] Z. Kutnjak, J. Petzelt, and R. Blinc, The giant electromechanical response in ferroelectric relaxors as a critical phenomenon, Nature (London, U.K.) **441**, 956 (2006).

[8] K. Uchino, *Piezoelectric Actuators and Ultrasonic Motors* (Kluwer Academic, Boston, 1996).

[9] M. Valant, Electrocaloric materials for future solid-state refrigeration technologies, Prog. Mater. Sci. **57**, 980 (2012).

[10] G. Xu, J. Wen, C. Stock, and P. M. Gehring, Phase instability induced by polar nanoregions in a relaxor ferroelectric system, Nat. Mater. **7**, 562 (2008).

[11] R. A. Cowley, S. N. Gvasaliya, S. G. Lushnikov, B. Roessli, and G. M. Rotaru, Relaxing with relaxors: A review of relaxor ferroelectrics, Adv. Phys. **60**, 229 (2011).

[12] V. V. Shvartsman, D. C. Lupascu, and D. J. Green, Lead-free relaxor ferroelectrics, J. Am. Ceram. Soc. **95**, 1 (2012).

[13] Y. Imry and S.-K. Ma, Random-Field Instability of the Ordered State of Continuous Symmetry, Phys. Rev. Lett. **35**, 1399 (1975).

[14] V. Westphal, W. Kleemann, and M. D. Glinchuk, Diffuse Phase Transitions and Random-Field-Induced Domain States of the "Relaxor" Ferroelectric $PbMg_{1/3}Nb_{2/3}O_3$, Phys. Rev. Lett. **68**, 847 (1992).

[15] R. Pirc and R. Blinc, Spherical random-bond-random-field model of relaxor ferroelectrics, Phys. Rev. B **60**, 13470 (1999).

[16] D. Fu, H. Taniguchi, M. Itoh, S.-Y. Koshihara, N. Yamamoto, and S. Mori, Relaxor $Pb(Mg_{1/3}Nb_{2/3})O_3$: A Ferroelectric with Multiple Inhomogeneities, Phys. Rev. Lett. **103**, 207601 (2009).

[17] V. V. Shvartsman, J. Zhai, and W. Kleemann, The dielectric relaxation in solid solutions $BaTi_{1-x}Zr_xO_3$, Ferroelectrics **379**, 77 (2009).

[18] U. Hochli and D. Baeriswyl, Coexisting polar configurations in potassium-lithium tantalate, J. Phys. C: Solid State Phys. **17**, 311 (1984).

[19] J. Toulouse, B. E. Vugmeister, and R. Pattnaik, Collective Dynamics of Off-Center Ions in $K_{1-x}Li_xTaO_3$: A Model of Relaxor Behavior, Phys. Rev. Lett. **73**, 3467 (1994).

[20] V. V. Shvartsman, W. Kleeman, J. Dec, Z. K. Xu, and S. G. Lu, Diffuse phase transition in $BaTi_{1-x}Sn_xO_3$ ceramics: An intermediate state between ferroelectric and relaxor behavior, J. Appl. Phys. **99**, 124111 (2006).

[21] A. R. Akbarzadeh, S. Prosandeev, E. J. Walter, A. Al-Barakaty, and L. Bellaiche, Finite-Temperature Properties of $Ba(Zr, Ti)O_3$ Relaxors from First Principles, Phys. Rev. Lett. **108**, 257601 (2012).

[22] D. Sherrington, $Pb(Mg_{1/3}Nb_{2/3})O_3$: A minimal induced-moment soft pseudospin glass perspective, Phys. Rev. B **89**, 064105 (2014).

[23] D. Sherrington, BZT: A Soft Pseudospin Glass, Phys. Rev. Lett. **111**, 227601 (2013).

[24] J. Hlinka, S. Kamba, J. Petzelt, J. Kulda, C. A. Randall, and S. J. Zhang, Diffuse scattering in $Pb(Zn_{1/3}Nb_{2/3})O_3$ with 8% $PbTiO_3$ by quasi-elastic neutron scattering, J. Phys.: Condens. Matter **15**, 4249 (2003).

[25] C. Stock, L. Van Eijck, P. Fouquet, M. Maccarini, P. M. Gehring, G. Xu, H. Luo, X. Zhao, J.-F. Li, and D. Viehland, Interplay between static and dynamic polar correlations in relaxor $Pb(Mg_{1/3}Nb_{2/3})O_3$, Phys. Rev. B **81**, 144127 (2010).

[26] Z. Xu, J. Wen, G. Xu, C. Stock, J. S. Gardner, and P. M. Gehring, Two-component model of the neutron diffuse scattering in the relaxor ferroelectric PZN-4.5%PT, Phys. Rev. B **82**, 134124 (2010).

[27] V. Bovtun, S. Kamba, A. Pashkin, M. Savinov, P. Samoukhina, J. Petzelt, I. P. Bykov, and M. D. Glinchuk, Central-peak components and polar soft mode in relaxor $PbMg_{1/3}Nb_{2/3}O_3$ crystals, Ferroelectrics **298**, 23 (2004).

[28] S. Kamba, V. Bovtun, J. Petzelt, I. Rychetsky, R. Mizaras, A. Brilingas, J. Banys, J. Grigas, and M. Kosec, Dielectric dispersion of the relaxor PLZT ceramics in the frequency range 20 Hz–100 THz, J. Phys.: Condens. Matter **12**, 497 (2000).

[29] A. Bussmann-Holder, A. R. Bishop, and T. Egami, Relaxor ferroelectrics and intrinsic inhomogeneity, Europhys. Lett. **71**, 249 (2005).

[30] A. Bussmann-Holder, The polarizability model for ferroelectricity in perovskite oxides, J. Phys.: Condens. Matter **24**, 273202 (2012).

[31] M. E. Manley, J. W. Lynn, D. L. Abernathy, E. D. Specht, O. Delaire, A. R. Bishop, R. Sahul, and J. D. Budai, Phonon localization drives polar nanoregions in a relaxor ferroelectric, Nat. Commun. **5**, 3683 (2014).

[32] W. Dmowski, S. B. Vakhrushev, I.-K. Jeong, M. P. Hehlen, F. Trouw, and T. Egami, Local Lattice Dynamics and the Origin of the Relaxor Ferroelectric Behavior, Phys. Rev. Lett. **100**, 137602 (2008).

[33] A. Pramanick, W. Dmowksi, T. Egami, A. S. Budisuharto, F. Weyland, N. Novak, A. D. Christianson, J. M. Borreguero, D. L. Abernathy, and M. R. V. Jørgensen, Stabilization of Polar Nanoregions in Pb-Free Ferroelectrics, Phys. Rev. Lett. **120**, 207603 (2018).

[34] H. Ogihara, C. A. Randall, and S. Trolier-McKinstry, Weakly coupled relaxor behavior of $BaTiO_3$-$BiScO_3$ ceramics, J. Am. Ceram. Soc. **92**, 110 (2009).

[35] M. A. Beuerlein, N. Kumar, T.-M. Usher, H. J. Brown-Shaklee, N. Raengthon, I. M. Reaney, D. P. Cann, J. L. Jones, and G. L. Brennecka, Current understanding of structure–processing–property relationships in $BaTiO_3$-$Bi(M)O_3$ dielectrics, J. Am. Ceram. Soc. **99**, 2849 (2016).

[36] S. Nayak, S. Venkateshwarlu, A. Setiadi Budisuharto, M. R. V. Jøergensen, O. Borkiewicz, K. A. Beyer, and A. Pramanick, Effect of *A*-site substitutions on energy storage properties of $BaTiO_3$-$BiScO_3$ weakly coupled relaxor ferroelectrics, J. Am. Ceram. Soc. **102**, 5919 (2019).

[37] H. Ogihara, C. A. Randall, and S. Trolier-McKinstry, High-energy density capacitors utilizing $0.7\,BaTiO_3$-$0.3\,BiScO_3$ ceramics, J. Am. Ceram. Soc. **92**, 1719 (2009).

[38] S. S. N. Bharadwaja, J. R. Kim, H. Ogihara, L. E. Cross, S. Trolier-McKinstry, and C. A. Randall, Critical slowing down mechanism and reentrant dipole glass phenomena in $(1-x)BaTiO_3$-$xBiScO_3$, $(0.1 \leqslant x \leqslant 0.4)$: The high energy density dielectrics, Phys. Rev. B **83**, 024106 (2011).

[39] S. S. N. Bharadwaja, S. Trolier-McKinstry, L. E. Cross, and C. A. Randall, Reentrant dipole glass properties in $(1-x)BaTiO_3$-$xBiScO_3$, $0.1 \leqslant x \leqslant 0.4$, Appl. Phys. Lett. **100**, 022906 (2012).

[40] I. Levin, V. Krayzman, J. C. Woicik, F. Bridges, G. E. Sterbinsky, T.-M. Usher, J. L. Jones, and D. Torrejon, Local structure in $BaTiO_3$-$BiScO_3$ dipole glasses, Phys. Rev. B **93**, 104106 (2016).

[41] V. Krayzman, I. Levin, J. C. Woicik, and F. Bridges, Correlated rattling-ion origins of dielectric properties in reentrant dipole glasses $BaTiO_3$-$BiScO_3$, Appl. Phys. Lett. **107**, 192903 (2015).

[42] L. Luisman, A. Feteira, and K. Reichmann, Weak-relaxor behaviour in Bi/Yb-doped $KNbO_3$ ceramics, Appl. Phys. Lett. **99**, 192901 (2011).

[43] K. Uchino and S. Nomura, Critical exponents of the dielectric constants in diffused phase-transition crystals, Ferroelectrics **44**, 55 (1982).

[44] T. R. Shrout and J. Fielding, Jr., Relaxor ferroelectric materials, Ultrason Symp. Proc. **2**, 711 (1990).

[45] See Supplemental Material at http://link.aps.org/supplemental/10.1103/PhysRevB.103.214105 for additional details for fitting of dielectric and x-ray PDF data, and XPS data for Sn 3*d* states; also see Refs. [46–49].

[46] J. F. Moulder, W. F. Stickle, P. E. Sobol, and K. D. Bomben, *Handbook of X-Ray Photoelectron Spectroscopy* (Perkin-Elmer Corporation, Eden Prairie, MN, 1992).

[47] National Institute of Standards and Technologies (NIST) XPS database; https://srdata.nist.gov/xps/Default.aspx

[48] S. Venkateshwarlu, S. Nayak, F. P. Marlton, F. Weyland, N. Novak, D. Maurya, Y. Veerabhadraiah, O. Borkiewicz, K. A. Beyer, M. R. V. Jørgensen, and A. Pramanick, Relaxor behavior and electrothermal properties of Sn- and Nb-modified (Ba, Ca)TiO_3 Pb-free ferroelectric, J. Mater. Res. **35**, 1017 (2020).

[49] S. Venkateshwarlu, L. K. Venkataraman, V. Segouin, F. P. Marlton, H. C. Hin, D. Chernyshov, Y. Ran, M. R. V. Jørgensen, S. Nayak, J. Rödel, L. Daniel, and A. Pramanick, Large electromechanical strain and unconventional domain switching near phase convergence in a Pb-free ferroelectric, Commun. Phys. **3**, 193 (2020).

[50] G. S. Fulcher, Analysis of recent measurement of the viscosity of glasses, J. Am. Ceram. Soc. **8**, 339 (1925).

[51] D. H. Vogel, Das temperaturabhaengigkeitsgesetz der viskositaet von fluessigkeiten, Phys. Z. **22**, 645 (1921).

[52] T. Egami, Local structure of ferroelectric materials, Annu. Rev. Mater. Res. **37**, 297 (2007).

[53] T. Egami and S. J. L. Billinge, *Underneath the Bragg Peaks* (Elsevier, Oxford, UK, 2012).

[54] C. L. Farrow, P. Juhás, J. W. Liu, D. Bryndin, E. S. Božin, J. Bloch, Th. Proffen, and S. J. L. Billinge, PDFFIT2 and PDFGUI: Computer programs for studying nanostructure in crystals, J. Phys.: Condens. Mater. **19**, 335219 (2007).

[55] R. Comes, M. Lambert, and A. Guinier, The chain structure of $BaTiO_3$ and $KNbO_3$, Solid State Commun. **6**, 715 (1968).

[56] R. Comes, M. Lambert, and A. Guinier, Désordre linéaire dans les cristaux (cas du silicium, du quartz, et des pérovskites ferroélectriques), Acta Crystallogr., Sect. A **26**, 244 (1970).

[57] I.-K. Jeong, T. W. Darling, J. K. Lee, Th. Proffen, R. H. Heffner, J. S. Park, K. S. Hong, W. Dmowski, and T. Egami, Direct Observation of the Formation of Polar Nanoregions in $Pb(Mg_{1/3}Nb_{2/3})O_3$ Using Neutron Pair Distribution Function Analysis, Phys. Rev. Lett. **94**, 147602 (2005).

[58] T.-M. Usher, T. Iamsasri, J. S. Forrester, N. Raengthon, N. Triamnak, D. P. Cann, and J. L. Jones, Local and average structures of $BaTiO_3$-$Bi(Zn_{1/2}Ti_{1/2})O_3$, J. Appl. Phys. **120**, 184102 (2016).

[59] G. Laurita, K. Page, S. Suzuki, and R. Seshadri, Average and local structure of the Pb-free ferroelectric perovskites (Sr, Sn)TiO_3 and (Ba, Ca, Sn)TiO_3, Phys. Rev. B **92**, 214109 (2015).

[60] C. Ang, Z. Yu, P. M. Vilarinho, and J. L. Baptista, Bi : $SrTiO_3$: A quantum ferroelectric and a relaxor, Phys. Rev. B **57**, 7403 (1998).

[61] J. Harada, J. D. Axe, and G. Shirane, Neutron scattering study of soft modes in cubic $BaTiO_3$, Phys. Rev. B **4**, 155 (1971).

[62] G. Shirane, J. D. Axe, and J. Harada, Inelastic neutron scattering from single-domain $BaTiO_3$, Phys. Rev. B **2**, 3651 (1970).

[63] A. A. Belik, S. Iikubo, K. Kodama, N. Igawa, S.-I. Shamoto, M. Maie, T. Nagai, Y. Matsui, S. Y. Stefanovich, B. I. Lazoryak, and E. Takayama-Muromachi, $BiScO_3$: Centrosymmetric $BiMnO_3$-type oxide, J. Am. Chem. Soc. **128**, 706 (2006).

[64] S. Trolier-McKinstry, M. D. Biegalski, J. Wang, A. A. Belik, E. Takayuma-Muromachi, and I. Levin, Growth, crystal structure, and properties of epitaxial $BiScO_3$ thin films, J. Appl. Phys. **104**, 044102 (2008).

[65] J. P. Sokoloff, L. L. Chase, and D. Rytz, Direct observation of relaxation modes in $KNbO_3$ and $BaTiO_3$ using ineleastic light scattering, Phys. Rev. B **38**, 597 (1988).

[66] A. Pramanick, X. P. Wang, C. Hoffmann, S. O. Diallo, M. R. V. Jørgensen, and X.-L. Wang, Microdomain dynamics in single-crystal $BaTiO_3$ during paraelectric-ferroelectric phase transition measured with time-of-flight neutron scattering, Phys. Rev. B **92**, 174103 (2015).